Inertia-gravity wave in the polar mesopause region inferred from successive images of a meteor train

Hidehiko Suzuki,[1] Takuji Nakamura,[2] Sharon L. Vadas,[3] Masaki Tsutsumi,[2] Makoto Taguchi,[1] and Yasunori Fujiwara[4]

Received 27 September 2012; revised 20 December 2012; accepted 27 January 2013; published 19 April 2013.

[1] A fireball meteor with a visual magnitude over −6 followed by a persistent train was observed by two all-sky cameras for detecting the aurora and sodium airglow at Syowa Station (69.0°S, 39.5°E), Antarctica, on 7 June 2008. The orbit and other parameters of the fireball were estimated with an all-sky television camera for detecting the aurora. After the passage of this fireball, a circular train in the Na airglow was observed. This train expanded to a diameter of about 50 km in 9 min. Assuming that the fireball contained and emitted Na, we found this ring to span the altitudes of $z = 76$ to 87 km. The ring's mean motion was most likely caused by a large-scale, inertia-gravity wave with a vertical wavelength of ~16 km and an amplitude of ~30 m/s in the mesopause region.

Citation: Suzuki, H., T. Nakamura, S. L. Vadas, M. Tsutsumi, and M. Taguchi (2013), Inertia-gravity wave in the polar mesopause region inferred from successive images of a meteor train, *J. Geophys. Res. Atmos.*, *118*, 3047–3052, doi:10.1002/jgrd.50228.

1. Introduction

[2] It is now known that atmospheric gravity waves play a major role in the dynamics of the mesopause and lower thermosphere (MLT) region [*Lindzen*, 1981; *Holton*, 1983; *Fritts et al*., 1994; *Fritts and Alexander*, 2003]. Many investigators have quantified the wind and/or wave structures of this region using rocket observations [e.g., *Lübken*, 1997; *Larsen*, 2002; *Larsen et al*., 2005; *Rapp et al*., 2004; *Chu et al*., 2007], incoherent scatter and meteor radars [e.g., *Clark et al*., 1999; *Nakamura et al*., 2002; *Nicolls et al*., 2010], optical imaging [e.g., *Taylor et al*., 1995; *Gardner et al*., 1999; *Yamada et al*., 2001], and lidars [e.g., *She et al*., 1991; *Collins et al*., 1994; *Zhao et al*., 2003; *Gardner and Liu*, 2007]. Tracing a meteor train using ground-based optics is another method to determine the wind field in the MLT region. Meteor trains are luminous clouds that are formed along the meteor orbits after the passage of bright meteors or fireballs [e.g., *Jenniskens et al*., 2000]. The altitudes of these meteor events range from 80 to 100 km. The occurrence of a long-lived meteor train up to tens of minutes, called a persistent train, is quite random and rare; however, such an event allows for a relatively long-duration observation of the wind field in the MLT region. In particular, the meteor train can be a tracer of waves that have a relatively large vertical wavelength, such as tidal waves and inertia-gravity waves, since the spread is over a large altitude range. Although statistical studies of these waves in the Antarctic MLT region have already been conducted by many researchers with more powerful, stable, and continuous methods, such as radars [i.e., *Murphy et al*., 2006] and lidars [i.e., *Collins et al*., 1994], the derivation of the wind from a meteor train is useful as a case study. One of the advantages of meteor train tracing is the high spatial-temporal resolution for deducing atmospheric parameters. For example, *Kelley et al*., [2003] estimated the eddy diffusion coefficient of a turbulent structure by measuring the evolution rate of the width of a persistent meteor train during the Leonid meteor stream using an image-intensified video camera with a narrow field of view. Another merit is its tolerance to electromagnetic disturbances in the upper atmosphere (i.e., aurora or charged particle precipitation). For example, wind data from the medium-frequency (MF) radar is less reliable when the D-region of the ionosphere is disturbed by an aurora event [i.e., *Tsutsumi et al*., 2001]. On the other hand, if a wavelength band that is free from strong auroral contamination is selected for a meteor train observation, the wind field in the MLT region can be estimated even during auroral activity.

[3] In this case study, we obtained successive images of a meteor train by an all-sky imager (ASI) for an airglow study. By analyzing the motion of the meteor train, we deduce the components of the wind mostly due to an inertia-gravity wave in the polar mesopause region under an auroral activity.

2. Instrumentation

[4] Syowa Station is located at 39.6°E and 69.0°S in the Antarctica and is a scientific observation base for various geophysical studies, including studies of the middle and upper atmosphere. Various optical instruments and radars observe aurora and airglow there. The data sets used in this study were obtained by an ASI for sodium airglow, an all-sky television camera (ATV), and an MF radar.

[1]Rikkyo University, College of Science, Toshimaku, Tokyo, Japan.
[2]National Institute of Polar Research, Tachikawa, Tokyo, Japan.
[3]NorthWest Research Associates, Boulder, Colorado, USA.
[4]Nippon Meteor Society, Yodogawa, Osaka, Japan.

Corresponding author: H. Suzuki, Rikkyo University, 3-34-1, Nishi Ikebukuro, Toshimaku, Tokyo, 171-9602, Japan. (hsuzuki@rikkyo.ac.jp)

2169-897X/13/10.1002/jgrd.50228

[5] The ASI is a sensitive camera equipped with a cooled charge-coupled device (CCD) sensor, a fish-eye lens ($f = 8$ mm, F# = 2.8), relay lens, and a band-pass interference filter with a peak transmittance of 64% at 589.3 nm and a bandwidth of 2.7 nm at full width at half maximum. This filter is designed to observe sodium emission D-lines from an airglow layer centered at 92 km altitude. This instrument operated with a 1 min exposure time every minute during nighttime between autumn and spring. Details of the ASI are described in *Taguchi et al*., [2004]. The ASI data are mainly used to observe the Na emission from the meteor train in this study.

[6] The ATV is a panchromatic all-sky TV camera which records the auroral morphology at a frame rate of 30 Hz. An image intensifier tube is installed in front of the sensor to enhance faint signals. The ATV data are used here to determine the parameters of the meteor fireball.

[7] The MF radar is a monostatic pulse radar with a peak transmitting power of 50 kW and an operation frequency of 2.4 MHz. This instrument can be used to determine the horizontal wind velocity (u and v) between 60 and 90 km altitude when the D-region ionosphere is not disturbed by an aurora [e.g., *Tsutsumi et al*., 2001]. In this study, the MF radar data are used to estimate the mean background wind during this event.

3. Observations Results

3.1. Meteor Parameters

[8] A meteor fireball was observed at 21:58:45 UT on 7 June 2008. The ATV video showed the meteor fireball starting at 21:58:45:58 UT. The fireball was observed in 40 successive frames, i.e., for 1.33 s. The maximum absolute magnitude of the fireball was estimated to be −6.2 by comparison with those of Jupiter (−2.6) and Alpha Centauri-A (0.0) on the ATV images. The fireball path was also recorded in one of the ASI images.

[9] We estimate the fireball orbit using temporal variation of the apparent angular velocity observed by the ATV (which has a frame rate of 30 s^{-1}) under the assumption that the meteor velocity V is constant. This assumption is appropriate because the deceleration of the meteor is much smaller than the variation of the apparent angular velocities due to the change of the orbit viewing angle. Here, the angle between the line-of-sight and the meteor orbit, denoted by B, as well as the actual meteor velocity, V, are determined by least squares method with an assumed initial altitude of H_0. We note that B does not depend on H_0, whereas V can vary by changing the assumed initial altitude H_0, the detail of which will be discussed latter. Details of the methods used to deduce a meteor orbit from a single camera observation are described in *Shiba* [1995].

[10] Unlike multistatic simultaneous observations where several ATV (or other) cameras can be used to determine the exact meteor altitude, we must estimate the altitude of this fireball from this single ATV camera. Here we assume a start altitude in our single station measurements to be $H_0 = 110$ km. This leads to a geocentric meteor velocity of $V = 69$ km/s and an angle of $B = 44°$. The deduced parameters are summarized in Table 1. Because the meteor is quite bright, it must be a large-mass meteor [*Mckinley*, 1961]. Note that the geocentric velocity is relatively large and is similar to those of the Leonid (70.7 km/s) and Orionid (66.4 km/s) meteor showers. Such high-speed meteor shower often shows meteors accompanied by bright persistent trains [*Kim et al*., 2004]. The average altitude of their maximum brightness is ~90 km for bright (large mass) meteors [*Koten et al*., 2004]; this closely corresponds to the altitude of maximum brightness in our case (88 km, Table 1). Thus, the initial height assumed in this estimate ($H_0 = 110$ km) is likely a good assumption. Although this method needs assumption of a height of the maximum or the initial brightening points, the offset error induced by this assumption of the start altitude only shifts estimated altitudes of the whole meteor orbit. For example, if the assumed initial meteor height is higher, the estimated ground velocity of the meteor and the altitudes of the meteor orbit shift to higher values. However, this does not affect the wind estimation described in the following sections because the relative horizontal distance between the meteor trains is not severely affected by a vertical shift of the whole meteor orbit.

Table 1. Estimated Parameters of the Fireball[a]

Parameter of the Fireball	Estimated Value
Geocentric velocity	69 km/s
Heliocentric velocity	34 km/s
Peak absolute magnitude	−6.2
Radiant point	
Right ascension (Ecliptic longitude)	347.0° (339.6°)
Declination (Ecliptic latitude)	−21.4° (−14.6°)
Sun ecliptic longitude	77.51°
Angle B (See text)	44°
Incident angle to the atmosphere	28.5° (depletion angle)
Beginning altitude (assumed)	110 km
Terminal altitude	74.8 km
Altitude of the peak brightness	88 km

[a] $H_0 = 110$ km is assumed.

3.2. Wind Determination

[11] In order to describe the images observed by ASI, we define the frame number of the image with the initial trace of the fireball to be frame #0. Figure 1 shows the trajectory of the fireball in frame #0. The fireball began at the east end (azimuth angle $\psi_s = 212.8°$, zenith angle $\chi_s = 24.6°$) of the bright region and terminated at the west end ($\psi_e = 123.0°$, $\chi_s = 28.6°$). The plus symbols show the locations of the fireball meteor trajectory from the ATV. The color shows intensity of the image (warmer color is more intense).

[12] The ASI observed luminous meteor trains with varying shape until frame #22, although the images after frame #9 are very faint. Figure 2b shows sequential difference images corresponding to frames #2 to #9 (~2 to 9 min after the fireball event). The horizontal scales of each image are the same as in Figures 1 and 2a. Note that the stars and bright galaxies are mostly removed by taking differential images of adjacent frames (i.e., the image of frame #3 is the photon counts of #3 minus those of #2). A portion of a ring (an arc) of a persistent train is seen 2 to 9 min after the fireball event. This train gradually expands in the radial direction. The approximate horizontal diameter of the ring is ~100 pixels in frame #9, corresponding to a horizontal distance of about 50 km if the structure is at around 87 km. The motion of the meteor train and the meteor orbit projected onto the horizontal plane is summarized in Figure 3. RMS

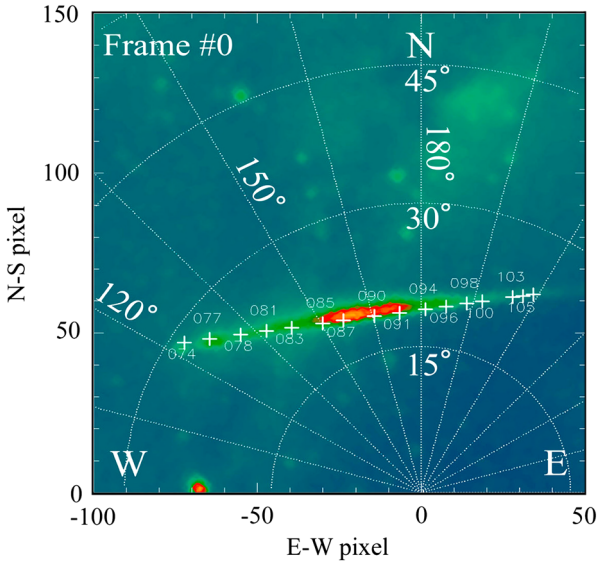

Figure 1. The meteor fireball trajectory in frame #0. Numbers shows zenith/azimuth angles in degrees. Pluses show the trajectory from the ATV. The color shows intensity in counts of the image (warmer color is much intense).

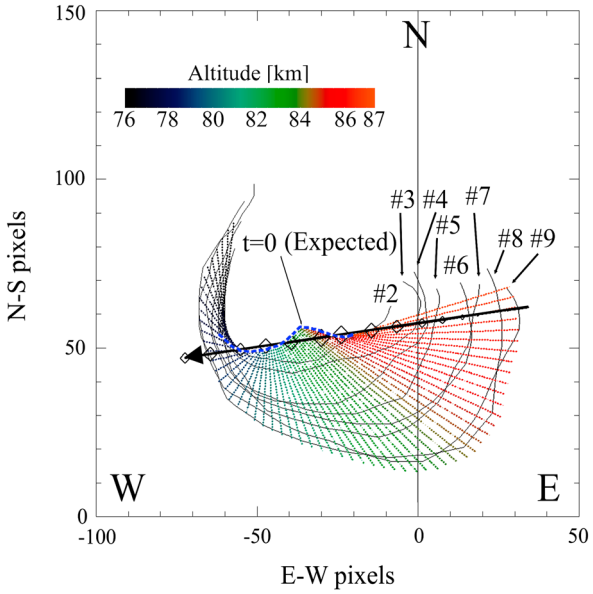

Figure 3. The meteor trajectory (solid line with arrow) and traces of the ring structure from frames #2 to #9 (thin solid lines). The vertical and horizontal axes show pixel number along S-N direction and W-E direction, respectively. The size of diamond symbol on the meteor trajectory shows relative brightness of the fireball. The blue dashed line shows the extrapolated initial shape from the estimated horizontal wind, using frames #2 and #9. The dotted lines with various colors show the extrapolated motion of each part of the structure. The difference of color shows estimated altitude of each train segment.

errors caused in determining the locations of the meteor train segments from the images are estimated to be 1.0 pixel. A basis of this 1.0 pixel error is justified in the next section.

[13] Figure 2a shows the clearest ring structure (frame #5). Note that this is not a different image but is a deviation from the image smoothed with a boxcar function with a size of 25×25 pixels. It should also be noted that this is a negative image where white and black colors show dark and bright parts of the airglow image, respectively. The black dots and regions mask Jupiter, stars, and the brightest portion of the Milky Way. The Milky Way is seen from the SW to NE in each image. The plus symbols show the trajectory of the meteor observed by the ATV and are in the same locations as in Figure 1. The white arrows point to the total visible extent of the ring structure.

[14] Meteors are known to contain sodium and to emit Na airglow as they travel downward in the Earth's atmosphere [*Millman*, 1953; *Jenniskens*, 2004]. Therefore, the train seen

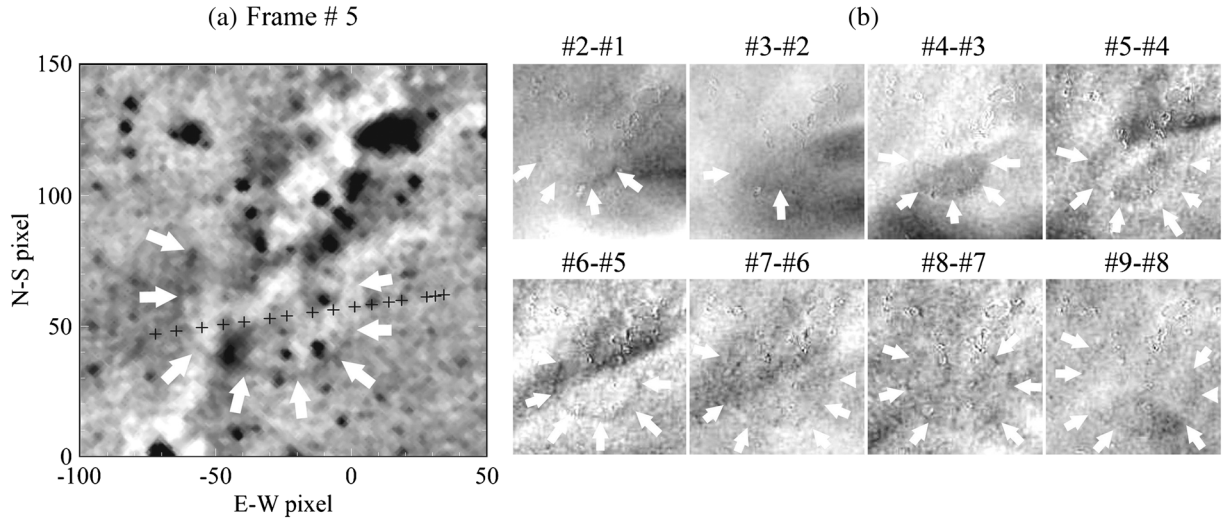

Figure 2. (a) The enlarged image of the ring structure is shown for frame #5. The deviation from the smoothed image is plotted as a negative image. (b) Sequential difference images corresponding to frames #2 to #9. The field of view of these images is the same as in Figure 2a. White arrows indicate positions of the meteor train.

in Figure 1 is not located at a single altitude but is instead spread out over a vertical distance; the northeastern edge is located at the highest altitude, while the northwestern edge is located at the lowest visible altitude.

[15] Since the persistent train is a "tracer" of the velocity of the particles in the atmosphere, we can infer the "background wind velocity" by tracking the displacement of the train in time from frame #2. For this calculation, we assume that the horizontal velocity at each altitude is constant during the event (i.e., 9 min). This is a good assumption if the period of the low-frequency wave is greater than an hour. We then note that the vertical velocity of a low-frequency wave is $w' = (l_z/l_H)u_H'$, where l_z and l_H are the vertical and horizontal wavelengths and u'_H is the horizontal velocity component of the lower frequency wave along its direction of propagation [*Fritts and Alexander*, 2003]. Since $l_z << l_H$ for a low-frequency wave, $w' << u_H'$. Therefore, we can neglect the vertical velocity contribution to the meteor train's motion for this "background wind" calculation and assume that the train only moves horizontally. Again, these are reasonable assumptions if the background wind is caused by tides and other large-scale, low-frequency waves. Under these assumptions, each part of the ring structure moves along a straight line in the horizontal plane.

[16] First, we define the crossing points between the initial meteor trajectory and the meteor train in each frame as shown in Figure 4a. Each pair of crossing points (at lower and higher altitudes) on the train in each image can be considered to be at the same altitude if the motion of each segment is approximately constant.

[17] Next, for frames #2 to #9, we divide the meteor train between the crossing points into a fixed number of equal length segments, as shown in Figure 4b. The train below and above the two crossing points is also divided into segments of the same length as those between the crossing points. Each segment is numbered in order from the lower crossing point, and then segments in different images with the same number are regarded as being at the same altitude.

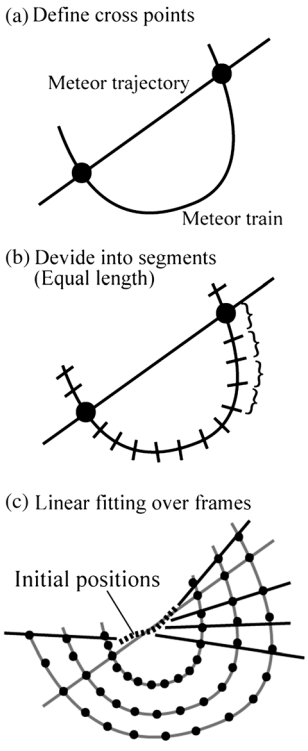

Figure 4. (a, b, c) Illustrations of the procedures to derive mean wind with meteor train images.

[18] The average horizontal velocity, $(v_{x\,i}, v_{y\,i})$, in image coordinates (pixels/s) together with the initial positions $(x_{0\,i}, y_{0\,i})$ of each segment are then simultaneously estimated by least squares fitting to the following linear functions:

$$x_i(t) = v_{x\,i}t + x_{0\,i} \tag{1}$$

$$y_i(t) = v_{y\,i}t + y_{0\,i} \tag{2}$$

where t is the time of each frame, and $(v_{x\,i}, v_{y\,i})$ and $(x_{0\,i}, y_{0\,i})$ are the average horizontal velocities and initial positions, respectively, of segment i. In this calculation, $(v_{x\,i}, v_{y\,i})$ and $(x_{0\,i}, y_{0\,i})$ are fitting parameters. The measurement error with a magnitude of 1.0 pixel in each segment corresponds to different error magnitudes in the horizontal location of the segments, depending on the zenith angle of the segment. These differences are taken into account to a weighting in the fitting. The concept behind this fitting method is illustrated in Figure 4c. The estimated initial position, $(x_{0\,i}, y_{0\,i})$, is shown by the blue dashed line in Figure 3. These points are aligned almost linearly and lie quite close to the initial meteor trajectory (black arrow in Figure 3). The distance between neighboring initial points is almost constant, which implies that the estimated average velocity represents the expanding motion of the meteor train well.

[19] The initial positions at $t = 0$ for the higher and lower crossing points are then used to derive the corresponding altitudes in the meteor trajectory, which are estimated to be 78.7 and 87.0 km, respectively.

[20] The altitudes of segments other than at the crossing points are determined by linear extrapolation and interpolation along the meteor train. We then convert each segment's positions $(x_i(t), y_i(t))$ and horizontal velocity $(v_{x\,i}, v_{y\,i})$ to those in actual space coordinates (e.g., km, m/s) using these altitudes. The estimated altitudes are displayed using different colors in Figure 3. Meteor trains below 76 or above 87.4 km are too faint to be able to determine their location or motion characteristics, so only results between these two altitudes are plotted in Figure 3.

[21] Figures 5a and 5b show the height profile of the calculated horizontal winds. The winds shown here represent average background winds over a 9 min interval, since we used equations (1) and (2) (with their constant-velocity assumptions) to determine the segment velocities. Figures 5a and 5b show zonal and meridional wind components, respectively, and Figure 5c shows their hodograph. Estimation errors due to 1.0 pixel measurement error are also indicated by horizontal lines in Figures 5a and 5b. In the hodograph (Figure 5c), these errors are indicated by both vertical and horizontal lines.

[22] We also show the 30 day (±15 days from the event) average "monthly" wind profiles, $\bar{u}$ and $\bar{v}$, as measured by the MF radar (dotted lines). Of course, it would be best to compare the deduced wind in Figures 5a and 5b with that observed by the MF radar during the same period. However, the wind data during this event is not available due to auroral contamination. Thus, the MF wind data shown here displays the monthly average horizontal wind instead.

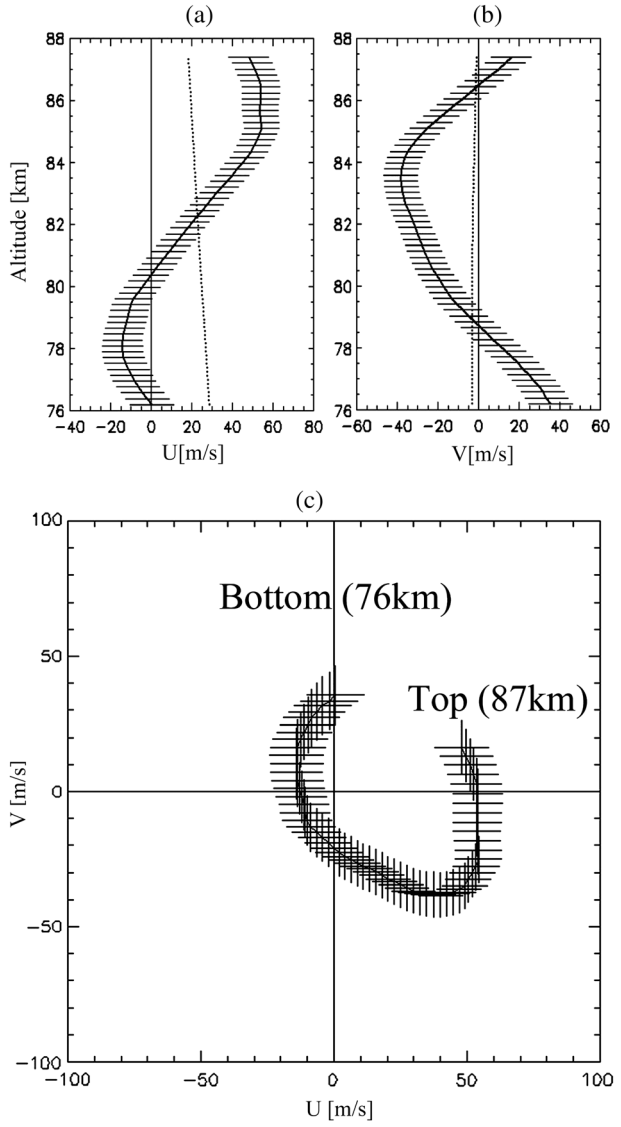

Figure 5. The estimated horizontal wind velocity profiles: (a) u (zonal wind) and (b) v (meridional wind), with errors shown as horizontal lines and MF wind velocities averaged over 30 days (±15 days from the event) shown in dotted lines; (c) a hodograph of u and v, with errors in fitting parameters shown as horizontal and vertical lines.

4. Discussion

[23] Figures 5a and 5b imply the presence of a tide or a large-scale, lower-frequency wave superimposed onto a mean wind whose amplitude is relatively constant with altitude. Figure 5b shows a wave with a meridional velocity component of $v' \sim 35$ m/s superimposed on a mean meridional wind. Similarly, Figure 5a shows the zonal wind component from this low-frequency wave with an amplitude of $u' \sim 30$ m/s superimposed on a mean zonal wind. We infer a half vertical wavelength of the wave to be about 8 km because the positive and negative peaks of u occur at altitudes of 86 and 78 km, respectively. Thus, the vertical wavelength of this wave is estimated to be about 16 km. Additionally, the hodograph in Figure 5c shows a counterclockwise rotation with altitude. This is the expected direction for an upward energy-propagating, inertia-gravity wave in the southern hemisphere [*Fritts and Alexander*, 2003]. Additionally, because the hodograph is nearly circular (roughly taking into account the growth of the wave's amplitude with altitude from the corresponding decrease in the mean density with altitude [*Fritts and Alexander*, 2003]), this suggests that the intrinsic wave period of this wave is near the inertial period [*e.g.*, *Yamamoto et al.*, 1987; *Nicolls et al.*, 2010]. According to multi-radar observations conducted in the Antarctic regions, a dominant tidal component near the latitude of Syowa Station is the semidiurnal tide with a zonal wave number of 2, which has a typical vertical wavelength of 76 km in June [*Murphy et al.* 2006]. This indicates that the vertical wavelength for our present case (16 km) is too short to be related to the tidal wave that is frequently observed during this same season. Therefore, the observed wave is most likely an inertia-gravity wave. Such waves can be created in the troposphere by changes in the flow of large air masses and have been observed in the northern polar mesosphere [e.g., *Yamamoto et al.*, 1987; *Nicolls et al.*, 2010]. Additionally, there is new evidence of stratospheric sources of inertia-gravity waves at high latitudes (C. Yamashita, personal communication, 2012). Although persistent trains are rare phenomena created only by bright meteors, several fine structures have been observed and reported. *Drummond et al.* [2001, 2002] and *Kruschwitz et al.*, [2001]reported imaging observations of persistent trains. They found remarkable persistent trains with peculiar shapes ("diamond ring," "glow worm") using high spatial resolution cameras and a sodium lidar at the Starfire Optical Range, New Mexico (35°N), during the period of the Leonid shower in 1998. The twisted persistent trains also showed clockwise rotation with the altitude. *Kim et al.*, [2004] observed an advective persistent train by an all-sky CCD airglow camera at Mt. Bohyum (36.2°N), Korea during the Leonid meteor shower in 2001. They also interpreted the motion of the train as being caused by advection from the background horizontal wind; this wind was found to be composed of an inertia-gravity wave and a mean wind. The horizontal wind vector associated with an upward energy-propagating inertia-gravity wave rotates clockwise with increasing altitude in the northern hemisphere because of the positive Coriolis parameter f.

5. Conclusions

[24] A fireball meteor event with a visual absolute magnitude of −6.2 and a geocentric velocity of ~69 km/s was detected by a highly sensitive all-sky television camera (ATV) at Syowa Station in Antarctica. A luminous ringlike train was detected by an all-sky sodium airglow imager (ASI) a few to 10 min after the fireball event. This meteor train had a nearly circular shape. It acted as a "tracer" of the underlying wind and generally expanded outward in time. Analysis of the train's motion allowed us to determine the horizontal velocity of the background wind from altitudes of 76 to 87 km. The derived average horizontal wind profiles implied the presence of an atmospheric wave with amplitudes of $u' \sim 30$ m/s and $v' \sim 35$ m/s and with a vertical wavelength of ~16 km. The nearly circular nature of the hodograph suggests that this wave had a period close to the inertial period. Counterclockwise rotation of horizontal

wind vector with altitude suggests that its energy propagated upward in time in the southern hemisphere. We therefore conclude that the expanding motion of the meteor train was most likely due to an upward-propagating, inertia-gravity wave.

[25] **Acknowledgments.** This work was supported by JSPS Grant-in-Aid for Scientific Research (B) (Grant Number 24340121) and National Institute of Polar Research Project Research No.KP-2. The Syowa ASI and MF radar are operated by the Science Program of JARE supported by NIPR, under MEXT. SLV was supported by NSF grants ATM-0836195 and AGS-1139149.

References

Chu, Y. H., C. L. Su, M. F. Larsen, and C. K. Chao (2007), First measurements of neutral wind and turbulence in the mesosphere and lower thermosphere over Taiwan with a chemical release experiment, *J. Geophys. Res.*, *112*, A02301, doi:10.1029/2005JA011560.

Clark, R.R, R.J. Tate, J.E. Salah and L.P. Goncharenko (1999), Common-volume measurements of mesospheric winds: 2. Small scale structure implications, *J. Atmos. Terr. Phys.*,*61*, 1273–1287.

Collins, R. L., A. Nomura, and C. S. Gardner (1994), Gravity waves in the upper mesosphere over Antarctica: Lidar observations at the South Pole and Syowa, *J. Geophys. Res.*, *99*(D3), 5475–5485, doi:10.1029/93JD03276.

Drummond, J. D., J. B. Grime, C. Gardner, A. Liu, X. Chu, and T. Kane (2001), Observations of persistent Leonid meteor trails 1. Advection of the "Diamond Ring", *J. Geophys. Res.*, *106*(A10), 21517–21524.

Drummond, J. D., J. B. Grime, C. Gardner, A. Liu, X. Chu, M. Kelly, C. Kruschwitz, and T. Kane (2002), Observations of persistent Leonid meteor trails 3. The "Glowworm", *J. Geophys. Res.*, *107*(A8), 1159.

Fritts, D. C., J. R. Isler, and Ø. Andreassen, (1994), Gravity wave breaking in two and three dimensions, 2. Three-dimensional evolution and instability structure, *J. Geophys. Res.*, *99*, 8109–8123.

Fritts, D. C., and M. J. Alexander, (2003), Gravity wavedynamics and effects in the middle atmosphere, *Rev. Geophys.*, *41*, 1–3.

Gardner, C. S., K. Gulati, Y. Zhao, and G. R. Swenson (1999), Measuring gravity wave momentum fluxes with airglow images, *J. Geophys. Res.*, *104*, 11,903–11,915.

Gardner, C. S., and A. Z. Liu (2007), Seasonal variations of the vertical fluxes of heat and horizontal momentum in the mesopause region at Starfire Optical Range, New Mexico, *J. Geophys. Res.*, *112*, D09113, doi:10.1029/2005JD006179.

Holton, J. R., (1983), The influence of gravity wave breaking on the general circulation of the middle atmosphere, *J. Atmos. Sci.*, *40*, 2497–2507.

Jenniskens P., M. Lacey, B. Allan, D. Self, and J. Plane (2000), FeO "orange arc" emission detected in optical spectrum of Leonid persistent train, *Earth, Moon Planets*, *82–83*, 471–488.

Jenniskens, P., (2004), Meteor induced chemistry, ablation products, and dust in the middle and upper atmosphere from optical spectroscopy of meteors, *Adv. Space Res.*, *33*, 1444–1454.

Kelley, M. C., C. A. Kruschwitz, C. S. Gardner, J. D. Drummond, and T. J. Kane (2003), Mesospheric turbulence measurements from persistent Leonid meteor train observations, *J. Geophys. Res.*, *108*(D8), 8454, doi:10.1029/2002JD002392.

Kim, Y. H., J. K. Chung, and Y. I. Won (2004), Observation of a persistent Leonid meteor train with an all-sky camera, *J. Atmos. Terr. Phys.*, *66*, 1001–1009.

Koten, P, J. Borovička, P. Spurný, H. Betlem, and S. Evans (2004), Atmospheric trajectories and light curves of shower meteors, *Astron. Astrophys.*, *428*, 683–690.

Kruschwitz, C., et al. (2001), Observations of persistent Leonid meteor trails 2. Photometry and numerical modeling, *J. Geophys. Res.*, *106*(A10), 21525–21541.

Larsen, M. F. (2002), Winds and shears in the mesosphere and lower thermosphere: Results from four decades of chemical release wind measurements, *J. Geophys. Res.*, *107*(A8), 1215, doi:10.1029/2001JA000218.

Larsen M. F., M. Yamamoto, S. Fukao, R. T. Tsunoda, and A. Saito, (2005), Observations of neutral winds, wind shears, and wave structure during a sporadic-E/QP event, *Ann. Geophys.*, *23*, 2369–2375.

Lindzen, R. S., (1981), Turbulence and stress owing to gravity wave and tidal breakdown, *J. Geophys. Res.*, *86*, 9707–9714.

Lübken, F.-J., (1997), Seasonal variations of turbulent energy dissipation rates at high latitudes as determined by in situ measurements of neutral density fluctuations, *J. Geophys. Res.*, *102*, 13,441–13,456.

Mckinley, D. W. R., Meteor science and engineering (1961), McGraw-Hill, New York.

Millman, P. M. (1953), The typical Perseid meteor spectrum, *Nature*, *172*, 853–854.

Murphy, D. J., et al., (2006), A climatology of tides in the Antarctic mesosphere and lower thermosphere, *J. Geophys. Res.*,*111*, D23104, doi:10.1029/2005JD006803.

Nakamura, T., S. Morita, T. Tsuda, H. Fukunishi and Y. Yamada (2002), Horizontal structure of wind velocity field around the mesopause region derived from meteor radar observations, *J. Atmos. Terr. Phys.*, *64*, 947–958.

Nicolls, M. J., R. H. Varney, S. L. Vadas, P.A. Stamus, C. J. Heinselman, R. B. Cosgrove, and M. C. Kelley, (2010), Influence of an inertia gravity wave on mesospheric dynamics: A case study with the Poker Flat Incoherent Scatter Radar, *J. Geophys. Res.*, *115*, D00N02.

Rapp, M., B. Strelnikov, A. Müllemann, F.-J. Lübken, and D. C. Fritts (2004), Turbulence measurements and implications for gravity wave dissipation during the MaCWAVE/MIDAS rocket program, *Geophys. Res. Lett.*, *31*, L24S07, doi:10.1029/2003GL019325.

She, C. Y., J. R. Yu, J. W. Huang, C. Nagasawa, and C. S. Gardner (1991), Na temperature lidar measurements of gravity wave perturbations of wind, density and temperature in the mesopause region, *Geophys. Res. Lett.*, *18*(7), 1329–1331,

Shiba, Y. (1995), Radiant point, trajectory and velocity from single photographic or TV observation, *Earth, Moon Planets*, *68*, 503–508.

Taguchi, M., M. Ejiri, and K. Tomimatsu (2004), A new all-sky optics for aurora and airglow imaging, *Adv. Polar Upper Atmos. Res.*, *18*, 140–148.

Taylor, M. J., M. B. Bishop, and V. Taylor (1995), All-sky measurements of short period waves imaged in the OI 557.7 nm, Na 589.2 nm, and near infrared OH and O2 (0,1) nightglow emissions, during the ALOHA-93 campaign, *Geophys. Res. Lett.*, *22*, 2833–2836.

Tsutsumi, M., T. Aso, and M. Ejiri (2001), Initial results of Syowa MF radar observations in Antarctica, *Adv. Polar Upper Atmos. Res.*, *15*, 103–116.

Yamada, Y., Fukunishi, H., Nakamura, T., Tsuda, T., (2001). Breakdown of small-scale quasi-stationary gravity wave and transition to turbulence observed in OH airglow, *Geophys. Res. Lett. 28*, 2153–2156.

Yamamoto, M., T. Tsuda, S. Kato, T. Sato, and S. Fukao (1987), A saturated inertia gravity wave in the mesosphere observed by the middle and upper atmosphere radar, *J. Geophys. Res.*, *92*, D10, 11993–11999

Zhao, Y., A. Z. Liu, and C. S. Gardner (2003), Measurements of atmospheric stability in the mesospause at Starfire optical range, NM, *J. Atmos. Sol. Terr. Phys.*, *65*, 219– 232.